Research Square

Preprints are preliminary reports that have not undergone peer review.
They should not be considered conclusive, used to inform clinical practice,
or referenced by the media as validated information.

Phonon Scattering and Thermal Resistance Allocation in β-Silicon Nitride Nanofilms under Large Temperature Gradients

Junnian Zhou
Xi'an Jiaotong University
Dian Huang
Xi'an Jiaotong University
Xuejie Li
Xi'an Jiaotong University
Jiachen Shi
Xi'an Jiaotong University
Feng Zhou
Xi'an Jiaotong University
Guihua Tang
Xi'an Jiaotong University
Zhibin Gao
Xi'an Jiaotong University
Wei Li
Xi'an Jiaotong University
Shengying Yue
syyue@xjtu.edu.cn

Xi'an Jiaotong University

Article

Keywords: silicon nitride, nanofilm, temperature gradient, three-phonon scattering, local-temperature mapping, thermal resistance

Posted Date: November 16th, 2026

DOI: https://doi.org/10.21203/rs.3.rs-11603353/v1

License: This work is licensed under a Creative Commons Attribution 4.0 International License.
Read Full License

Additional Declarations: No competing interests reported.

Phonon Scattering and Thermal Resistance Allocation in β-Silicon Nitride Nanofilms under Large Temperature Gradients

Abstract

Large temperature drops across nanofilms raise the question of how temperature-dependent phonon scattering distributes thermal resistance within a film of uniform composition. We combine nonequilibrium *ab initio* molecular dynamics with periodic-crystal phonon calculations for a 2.818 nm β-silicon nitride (β-Si_3N_4) film. Isothermal phonon responses are evaluated at actual layer temperatures to construct a mode-resolved local-temperature reference. Two independent trajectories sustain temperature differences of 446–465 K over an internal interval of 1.832 nm, with fitted gradients of 198–211 K nm^{-1}. For an acoustic mode with a thickness-matched wavelength of 2.827 nm, the mapped three-phonon rate decreases by 33.4% and 33.6% from hot to cold. Its conductivity contribution increases by factors of 1.496 and 1.501, primarily due to the longer phonon lifetime. Summing over all modes in the relaxation-time approximation gives a similar relative enhancement. Modes below 15 THz supply 91.8%–92.5% of the reference thermal conductivity along the film normal at the internal layers. Integrating the reciprocal reference conductivity yields an internal area-normalized reference resistance of approximately 4.57×10^{-11} m^2 K W^{-1}. About 54% is allocated to the hotter half of the internal interval. Vibration–potential spectra, spatial fluctuation amplitudes, and fixed-bin information entropies characterize the associated microscopic thermal states. This local-temperature description connects modal phonon relaxation to spatial conductivity variations and resistance allocation within a film of uniform composition.

Keywords: silicon nitride; nanofilm; temperature gradient; three-phonon scattering; local-temperature mapping; thermal resistance

1 Introduction

Thin protective layers distribute the temperature drop between an externally heated surface and a cooler load-bearing structure. In aeroengines, gas turbines, and flight surfaces, this distribution affects substrate temperature, thermal-expansion mismatch, and cyclic damage. Studies of thermal barrier coatings therefore connect insulation with phase stability and multilayer durability [1–4]. Advanced nuclear-energy components face a related temperature-control problem together with irradiation and environmental effects [5]. Measurements of irradiated ceramics have linked thermal-transport changes to lattice swelling and defects [6,7]. Fig. 1 places these applications in a common through-thickness heat-transfer geometry. At the nanometer scale, a large temperature drop can place different parts of one layer at different thermal states. Relating those states to phonon relaxation is important for understanding where resistance accumulates within the layer.

Silicon nitride combines a strong covalent network, low thermal expansion, and useful high-temperature mechanical properties. Crystal phase, grain morphology, and grain-boundary

composition govern its thermomechanical response [8]. High-temperature studies connect microstructure with creep, oxidation, and thermal-shock behavior [9–11]. Sintering additives, corrosive atmospheres, and oxide volatilization further affect the stability of protective layers [12,13], alongside stresses within thin films and multilayers [14]. Its thermal conductivity is also sensitive to structure: seed-assisted processing and elongated-grain alignment produce anisotropic transport [15], while lattice oxygen, impurities, and defects introduce scattering sources [16–18]. These findings make silicon nitride relevant both to heat removal and to temperature-drop allocation. The transport response must be specified for the crystal structure and thermal state under consideration.

Single-crystal calculations resolve this response at the phonon-mode level. Molecular dynamics calculations for α- and β-silicon nitride identify phase and directional differences [19]. First-principles calculations for β-silicon nitride (β-Si_3N_4) give room-temperature conductivities of approximately 169 and 57 W m^{-1} K^{-1} along the *c* and *a* axes, respectively, and relate relaxation to three-phonon scattering phase space and anharmonicity [20,21]. At film scales, boundaries, interfaces, propagation lengths, and structural disorder introduce dependencies on geometry and preparation [22,23]. Bogner and co-workers measured conductivities of 0.8–1.7 W m^{-1} K^{-1} in 300–1000 nm silicon nitride films [24]. In a 50 nm amorphous film, Alam and co-workers reported a decrease from 2.7 to 0.34 W m^{-1} K^{-1} as tensile strain increased to approximately 2.4% [25]. More recently, deposition-dependent crystallization and thermal properties were demonstrated in amorphous silicon nitride films exposed to high temperatures [26]. These studies distinguish intrinsic crystal responses from preparation, microstructural, and size effects.

Spatially varying transport can arise from changes in structure or thermal state. Strain gradients in III–V semiconductors, for example, modify phonon spectra and scattering [27]. In a film with fixed composition and harmonic properties, a temperature gradient instead samples different thermal excitations and relaxation rates at different positions. The phonon Boltzmann transport equation relates conductivity to mode heat capacities, group velocities, and lifetimes [28]. The anharmonic model determines the temperature response: four-phonon scattering, force-constant renormalization, and defects can alter calculated conductivities [29,30]. Phonopy and ShengBTE provide the harmonic and anharmonic quantities for a specified model [31,32]. Evaluating their isothermal response functions at actual layer temperatures defines a local-temperature reference. Modal summation gives the conductivity reference, and integrating its reciprocal gives the area-normalized resistance along the heat-transfer direction [33]. The unresolved question is how these modal responses combine to allocate resistance along a nanoscale temperature field.

Nonequilibrium atomistic dynamics supplies the layer temperatures for this description. The kinetic-energy-exchange method of Müller-Plathe establishes a heat current between source and sink regions [34]. Its first-principles implementation couples controlled energy transfer to self-consistent electronic-structure calculations, forming nonequilibrium *ab initio* molecular dynamics (NEAIMD) [35,36]. Atomic motion and the local electronic environment can then be examined alongside the temperature field. Vibration–potential spectra and element-resolved

statistics have characterized the connection between atomic motion and potential fluctuations in diatomic semiconductors [37]. These observables describe microscopic thermal states, while anharmonic phonon calculations supply the relaxation rates used for transport. Keeping these roles distinct connects the temperature-field analysis to microscopic fluctuations through explicit physical quantities.

Here, two independent NEAIMD trajectories provide actual layer temperatures in a β-Si_3N_4 nanofilm. Isothermal periodic-crystal phonon responses are evaluated along each field. An acoustic mode with a wavelength close to the film thickness separates heat-capacity and lifetime effects at fixed wave vector and branch. Summation over the full spectrum in the relaxation-time approximation (RTA) gives the reference thermal conductivity along the film normal. Its reciprocal and spatial integral resolve internal resistivity and resistance allocation. Vibration–potential spectra, spatial fluctuation amplitudes, and fixed-bin Shannon information entropies characterize the associated microscopic states. This analysis relates temperature-dependent phonon relaxation to conductivity contrast and model temperature-drop shares within a film of uniform composition.

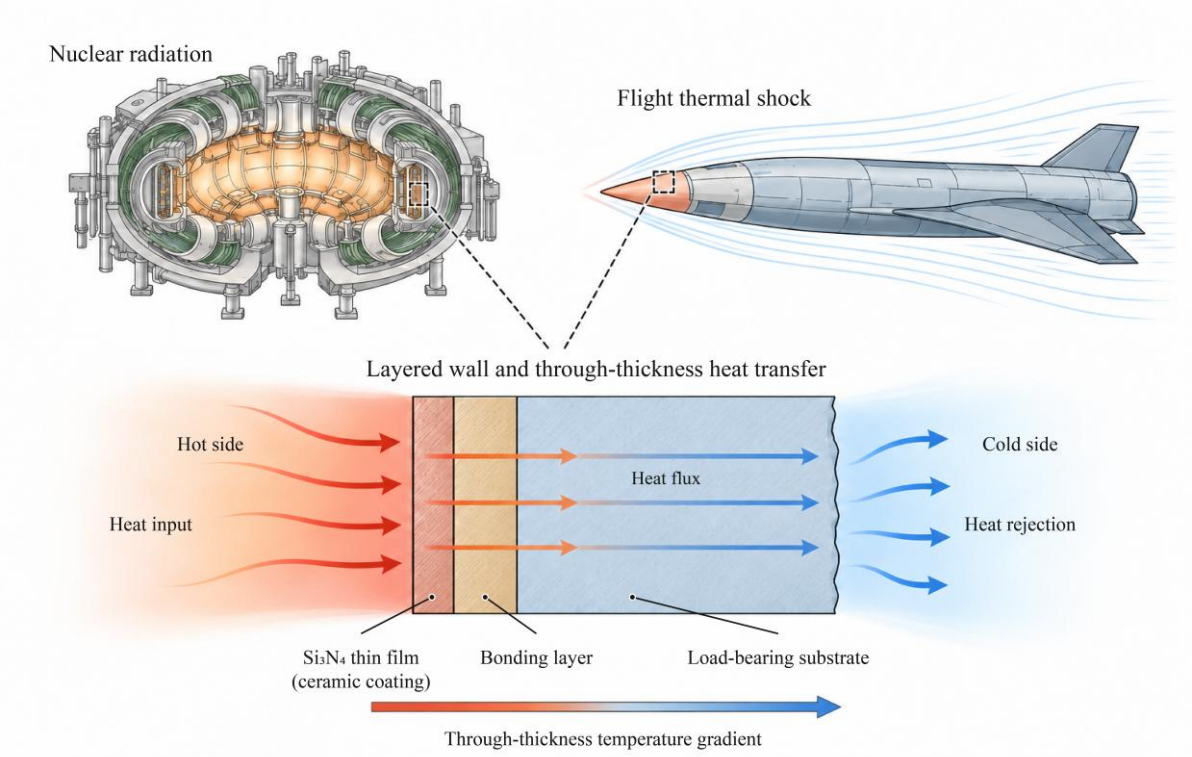


Fig. 1 Through-thickness heat transfer under high thermal loads. Nuclear-radiation-related and flight-thermal-shock settings are linked to a conceptual two-dimensional section of a Si_3N_4 film, bonding layer, and supporting substrate. Heat flows from left to right, with warm and cool colors identifying the thermal states. Conceptual artwork was prepared with OpenAI image-generation assistance

2 Results and discussion

2.1 Spatial thermal states within the film

The film geometry in Fig. 2a supports a substantial temperature contrast within the internal interval. Trajectory 1 in Fig. 2b falls from 1436.24 to 971.65 K, whereas trajectory 2 in Fig. 2c falls from 1373.33 to 927.26 K. The respective endpoint drops are 464.60 and 446.07 K across 1.832 nm; fits to all 14 internal means give gradient magnitudes of 211.3 and 198.0 K nm^{-1}. Local irregularities remain, but both trajectories place material of the same composition at markedly different thermal states over a nanometer-scale distance.

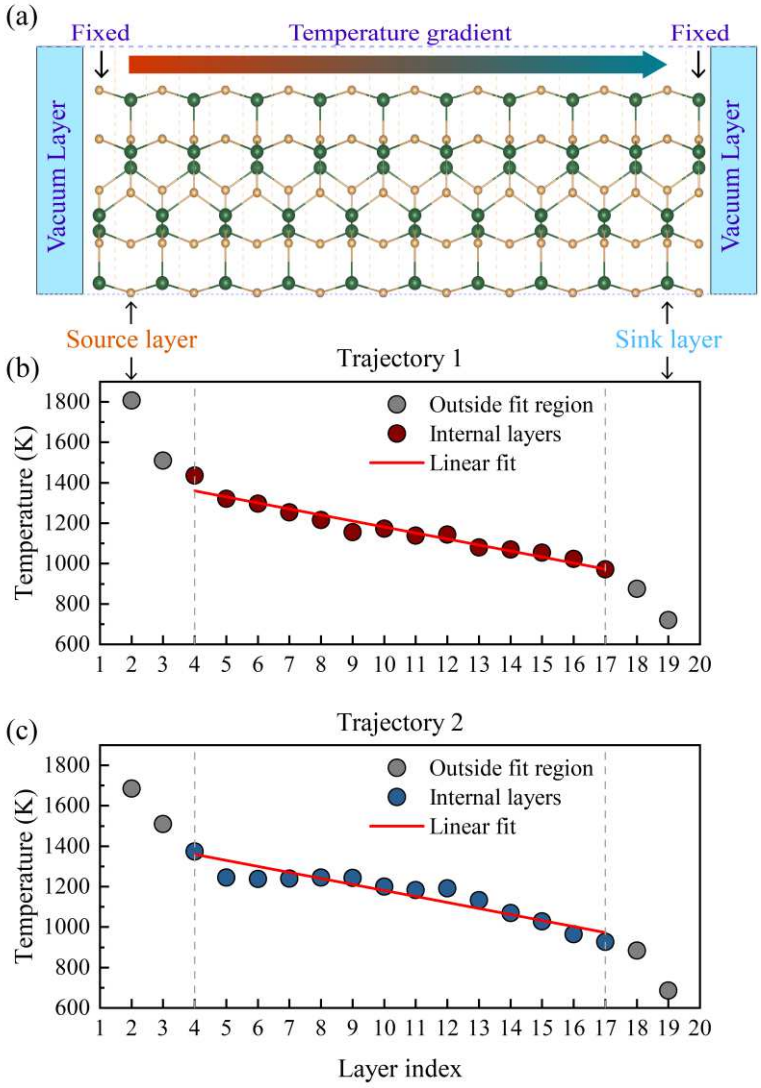


Fig. 2 Film model and layer temperatures. (a) Fixed end layers, vacuum regions, and source–sink arrangement. (b,c) Actual layer means for trajectories 1 and 2. Colored symbols identify internal layers 4–17, and gray symbols denote mobile layers outside the fit. Dashed lines mark the internal endpoints; red lines are linear fits. Material thickness and internal analysis length are 2.818 and 1.832 nm, respectively

Differences in layer kinetic energy specify the thermal states sampled by the spatial relaxation analysis. Continued source–sink energy exchange maintains their hot-to-cold ordering, while the actual means retain local variations from finite-time atomic motion. The fitted gradient describes the overall thermal driving; the individual layer temperatures determine where the response functions are evaluated. The broad contrast and local structure of the field thus supply complementary spatial information for the conductivity mapping.

Anharmonic relaxation provides the link between these thermal states and the conductivity response. The hot- and cold-side enlargements in Fig. 3 depict the qualitative contrast between stronger and weaker thermal motion. With harmonic frequencies and velocities fixed, temperature enters the periodic-crystal contribution through heat capacity and lifetime. The periodic-crystal RTA conductivity along the film normal is denoted by $\kappa_{zz}^{\mathrm{RTA}}(\mathrm{T})$, and its value at the layer temperature T(r) defines $\kappa_{zz}^{\mathrm{ref}}(\mathrm{r})$, abbreviated as κ^{ref}. The subscript zz denotes the film-normal tensor component; the superscripts RTA and ref distinguish the isothermal all-mode response and its local-temperature evaluation. The coordinate r increases from the internal hot-side endpoint toward the cold side, with r=0 at the first internal layer center. Evaluating that response along the layer field gives

$$\frac{d\kappa_{zz}^{ref}}{dr} = \frac{d\kappa_{zz}^{RTA}}{dT}\frac{dT}{dr} \tag{1}$$

This relation combines the temperature sensitivity of the material with the gradient sampled by the actual field. Over the present range, periodic-crystal RTA conductivity decreases with increasing temperature, giving an overall increase in κ^{ref} toward the colder endpoint. Local temperature plateaus and irregularities are retained in the spatial reference. The extent of the contrast depends jointly on the sampled thermal range and the response of the mode population. The two trajectories supply slightly different temperature paths along which the same response functions can be evaluated.

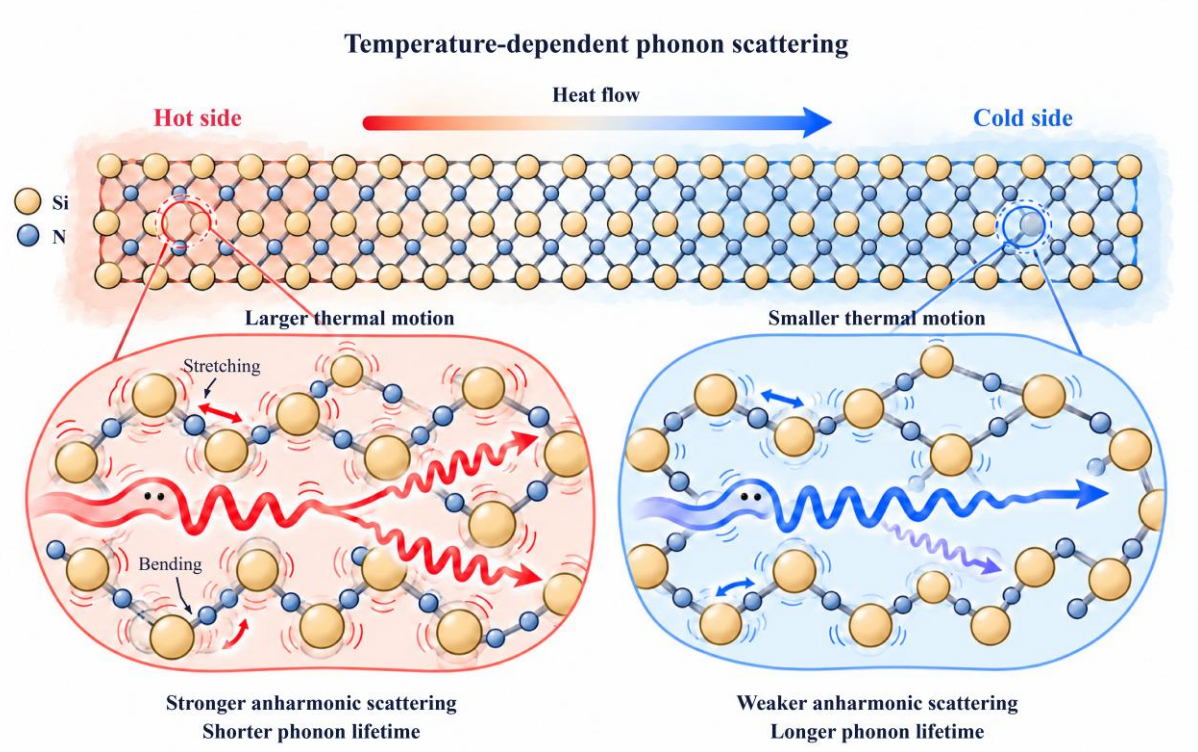


Fig. 3 Qualitative temperature dependence of anharmonic scattering. Heat flows from left to right. Enlarged hot and cold regions contrast thermal motion, scattering strength, and lifetime. The network, motion marks, and branching wave packets illustrate thermal excitation and scattering in a Si–N network. Conceptual artwork was prepared with OpenAI image-generation assistance

Heat capacity and lifetime play distinct roles in that response. The former measures the modal energy response to temperature; the latter characterizes relaxation through scattering. Their product, weighted by the squared normal velocity, determines the conductivity contribution. A fixed-mode analysis first separates these thermal factors, after which the complete spectrum establishes how the responding modes contribute to overall heat transfer.

2.2 Lifetime control of the thickness-matched mode

A fixed thickness-matched mode separates heat-capacity and lifetime effects without changing the wavelength under comparison. Fig. 4a locates this reference on the third acoustic branch from the Brillouin-zone center Γ toward A along the *c* axis, at a frequency of 4.259 THz and a normal group velocity of 10.73 km s^{-1}. The other two acoustic branches are nearly degenerate along this direction. Its wavelength of 2.827 nm places the reference close to the material-thickness scale.

Lifetime controls most of the temperature response. In Fig. 4b, the heat capacity normalized to its 300 K value approaches saturation, while the total lifetime and modal contribution decrease along nearly overlapping curves. Table 1 gives a three-phonon lifetime of 69.01 ps at 300 K, 13.89 ps at 1200 K, and 8.23 ps at 2000 K; the total lifetime at 1200 K is 13.85 ps. With

frequency and velocity fixed, the stronger lifetime reduction dominates the smaller heat-capacity increase, lowering the conductivity contribution.

The heat-capacity plateau indicates that thermal excitation of the reference acoustic mode is already substantial in this range. Further heating changes its energy response only slightly, whereas the continuing lifetime reduction suppresses its conductivity contribution. The nearly overlapping normalized curves follow from this difference in sensitivity. Because the wave vector, branch, and integration weight remain fixed, the comparison isolates the relative thermal responses of heat capacity and relaxation at a wavelength close to the film thickness.

The channel decomposition in Fig. 4c attributes that change primarily to anharmonic scattering. The three-phonon scattering rate I^{3ph} rises from 0.01449 ps^{-1} at 300 K to 0.07200 ps^{-1} at 1200 K and 0.12144 ps^{-1} at 2000 K, whereas the isotope term remains approximately 2.158×10^{-4} ps^{-1}. The three-phonon share consequently increases from 98.53% to 99.82% of the total rate. It dominates both relaxation and its temperature sensitivity for this mode.

Three-phonon processes connect modes through anharmonic combination and decay events, whose occupation factors increase with thermal excitation [32]. Natural-isotope scattering instead follows the mass disorder and harmonic modes and remains temperature independent within the fixed harmonic model [38]. At high temperature, the total rate therefore closely follows the anharmonic term, with a corresponding inverse change in lifetime. Applied along a cooling layer field, this channel balance predicts longer relaxation and a larger modal conductivity contribution toward the sink.

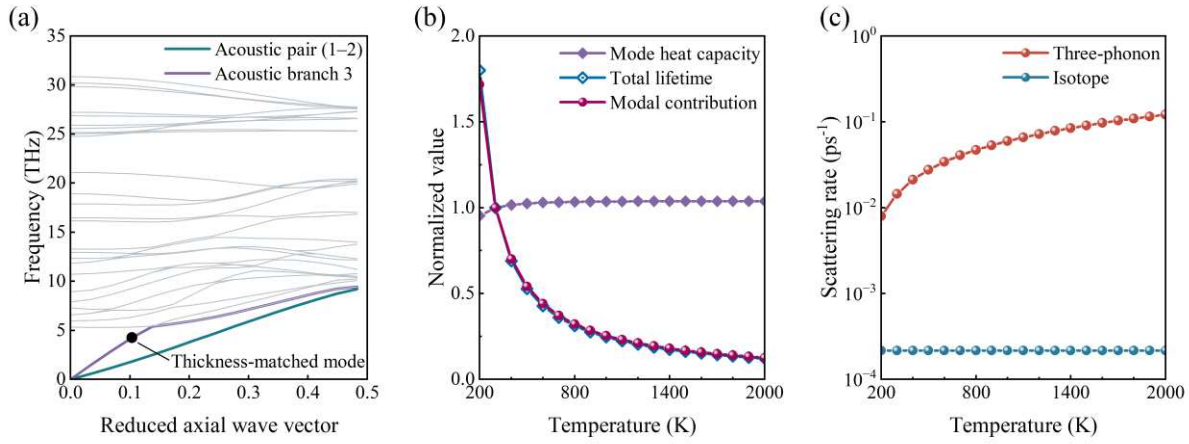


Fig. 4 Isothermal response of the thickness-matched acoustic mode. (a) Dispersion along Γ–A; acoustic branches are colored and the black point marks the reference at reduced wave vector (0,0,3/29). (b) Mode heat capacity, total lifetime, and single-mode conductivity contribution, each normalized to its own 300 K value. (c) Three-phonon and isotope rates; both channels enter the total lifetime

Table 1. Isothermal lifetimes and conductivity contributions of the thickness-matched mode.

Temperature (K)	Three-phonon lifetime (ps)	Total lifetime (ps)	Single-mode contribution (W m^{-1} K^{-1})
300	69.01	68.00	0.12313
600	29.26	29.07	0.05419
1200	13.89	13.85	0.02600
2000	8.23	8.22	0.01546

At 1200 K, broadening scale factors of 0.8 and 1.2 change the modal contribution by less than 0.55% relative to the baseline. The corresponding change in all-mode RTA conductivity along the film normal is less than 0.083%. The response is stable within the tested broadening interval. The reference mode carries the integration weight of a single full-zone point, so its relative change describes the temperature response at a fixed modal scale. Full spectral summation establishes the collective response of modes with different frequencies and propagation velocities.

2.3 Distinct mode-count and heat-carrying weights

The full spectrum retains the direction of the reference-mode response but reveals strongly unequal transport weights across frequency. In Fig. 5a, the *c*-axis RTA conductivity decreases from 177.89 W m^{-1} K^{-1} at 300 K to 38.78 at 1200 K and 23.14 at 2000 K, remaining above the *a*-axis value. Direction-dependent propagation and relaxation jointly produce the anisotropy, and the *c*-axis response is therefore used for mapping along the film normal.

This ordering extends the stronger *c*-axis transport reported for single-crystal β-Si_3N_4 [19–21]. Heat capacities approach saturation at high temperature, while increasingly rapid anharmonic scattering continues to reduce conductivity along both directions. Evaluating this response at actual layer temperatures assigns a lower reference conductivity to hotter layers and a higher value to colder layers. The directional analysis identifies the appropriate material response for the film normal; frequency resolution then identifies the modes carrying that response.

The conductivity decrease accompanies faster scattering throughout the main frequency bands, and Fig. 5b resolves substantial differences among modes at similar frequencies. The Si- and N-projected phonon densities of states (DOS) in Fig. 5c share a harmonic gap at 21.1041–24.7566 THz, above which lies a group containing 38.10% of all modes. Fig. 5d further resolves the propagation capacity of this group, with a median absolute normal velocity of approximately 0.57 km s^{-1}, compared with approximately 2.00 km s^{-1} below 15 THz. The squared-velocity factor in conductivity gives these slower high-frequency modes a relatively small normal transport weight.

The projected densities resolve the participation of Si and N in the vibrational spectrum, while group velocity measures the ability of each mode to propagate energy in the normal direction. A substantial high-frequency population can consequently coexist with a small normal transport weight. Heat capacity and lifetime provide further modal weighting. Comparing the density of states, rates, and velocities on the same frequency axis separates a numerically abundant set of vibrations from the modes responsible for most of the conductivity.

The continuous spectrum in Fig. 5e places the dominant conductivity at low and intermediate frequencies, where increasing temperature markedly reduces the absolute contributions. The unbroadened cumulative sum in Fig. 5f quantifies their relative shares: modes below 15 THz contribute 96.59%, 92.04%, and 91.61% at 300, 1200, and 2000 K, while the high-frequency group contributes only 0.45%, 2.87%, and 3.16%. The 50% cumulative frequency shifts from 7.17 to 7.83 THz between 300 and 2000 K, and the 90% frequency from 12.63 to 14.23 THz. Thus, declining absolute conductivity coexists with modestly broader normalized spectral coverage. The 4.259 THz reference belongs to the main heat-carrying range, within which modes with different velocities and lifetimes still contribute unequally.

The high-frequency fraction increases because temperature suppresses the absolute contributions of different bands by different amounts. The continuous spectrum gives absolute conductivity, while a normalized fraction measures its share of the total. As low- and intermediate-frequency contributions fall, the relative high-frequency share increases, yet modes below 15 THz still carry more than nine tenths of the total. The subsequent spatial contrast is therefore concentrated in existing low- and intermediate-frequency bands, through their temperature-dependent lifetimes and full modal weights.

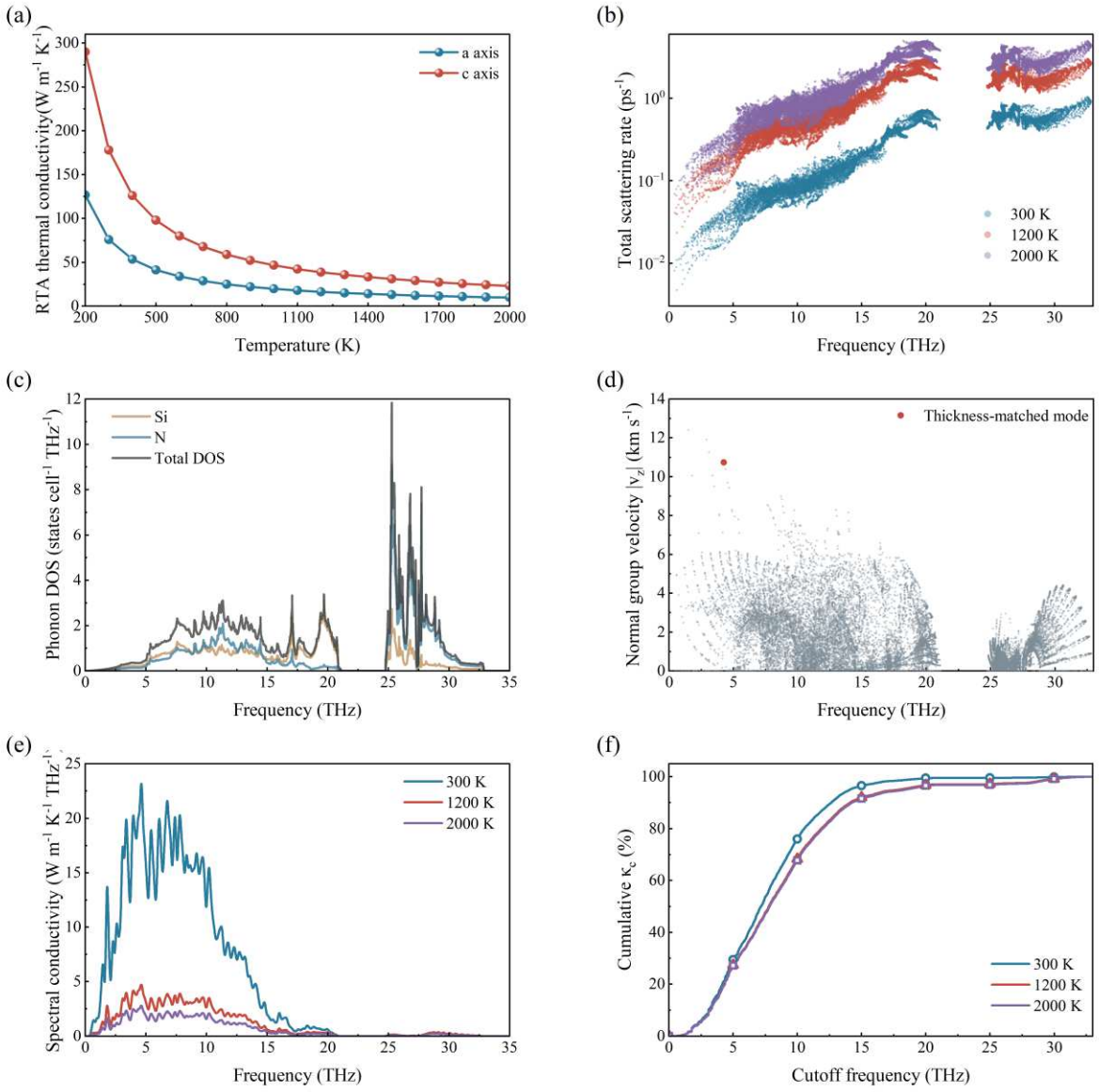


Fig. 5 Vibrational spectrum and RTA transport of periodic β-Si_3N_4. (a) Conductivity along a and c. (b) Total modal rates at 300, 1200, and 2000 K. (c) Si-projected, N-projected, and total densities of states per 14-atom cell. (d) Absolute normal group velocity; the red point marks the reference mode. (e) Gaussian-kernel *c*-axis conductivity spectrum with σ=0.10 THz. (f) Normalized cumulative *c*-axis conductivity from the original modal sum. Rate and velocity scatter plots display irreducible modes; transport integrals retain full-zone weights

2.4 Scattering distributions along the actual thermal field

The actual layer temperatures translate the isothermal scattering response into a spatial distribution of relaxation rates over the 1.832 nm internal interval. The normalized mode-count density p_Γ in Fig. 6a has two main concentrations that shift toward lower rates from hot to cold. Low- and intermediate-frequency modes dominate the lower-rate peak. Near the higher-rate peak, the conditional high-frequency share is approximately 74%–75%, with continued overlap

from modes below the gap. All layers share the same harmonic mode set, frequency-group populations, normalization, and kernel bandwidth. The spatial shift therefore reflects a redistribution of the same modes along the scattering-rate axis.

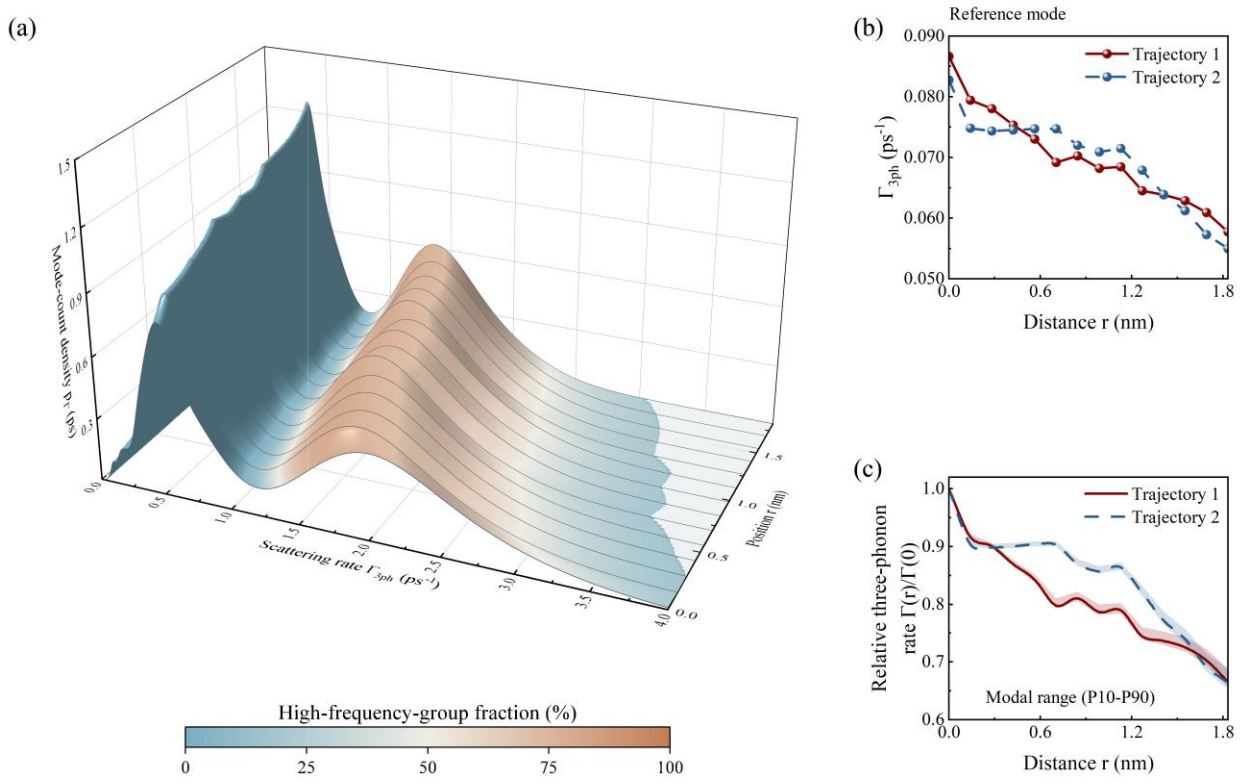


Fig. 6 Local-temperature mapping of the three-phonon rate distribution. (a) Mode-count density p_Γ for trajectory 1, integrating to one at each layer; color denotes the conditional count fraction of modes with f≥24.7566 THz near a given scattering rate. Curves mark the 14 actual layer centers. (b) Absolute reference-mode rates. (c) Count-weighted median rates of all positive-frequency modes relative to their own hot-side values, with 10th–90th percentile (P10–P90) ranges across modes. r=0 is the internal hot-side endpoint

The reference mode follows this population response. Fig. 6b gives a decrease in Γ^{3ph} from 0.08666 to 0.05774 ps^{-1} in trajectory 1 and from 0.08276 to 0.05496 ps^{-1} in trajectory 2. The respective reductions are 33.4% and 33.6%. Fig. 6c compares every positive-frequency mode with its own hot-side rate. The labels P10, P50, and P90 denote the count-weighted 10th percentile, median, and 90th percentile across modes. At the cold endpoint, the count-weighted P10/P50/P90 ratios are approximately 0.657/0.666/0.688 and 0.653/0.663/0.688. The median reduction of about one third places the selected mode within a broader response across frequencies and branches. Local variations in the actual temperature field remain visible in the absolute and relative rates, alongside this overall decrease.

The transport consequence depends on each mode's heat-carrying weight as well as its scattering rate. The high-frequency group contains 38.10% of all modes but contributes only 2.60%–3.00% of the reference thermal conductivity along the film normal at the internal layers. Modes below

15 THz supply 91.84%–92.45%. The count density describes the distribution of relaxation rates, while heat capacity, squared velocity, and lifetime determine each mode's conductivity contribution. Their combination distinguishes the modes that dominate a scattering-rate distribution from those responsible for most of the heat conduction.

2.5 Conductivity contrast and resistance allocation

Reduced scattering increases conductivity toward the cold side, with the longer lifetime controlling the reference-mode response. In Fig. 7a, its contribution rises from 0.02163 to 0.03235 W m^{-1} K^{-1} for trajectory 1 and from 0.02264 to 0.03397 W m^{-1} K^{-1} for trajectory 2. The cold-to-hot ratios are 1.496 and 1.501. Fig. 7b gives total-lifetime ratios of approximately 1.499 and 1.504, while heat-capacity ratios remain approximately 0.998. The lifetime increase therefore accounts for nearly all of the modal conductivity enhancement. Full spectral summation gives similar all-mode conductivity ratios of 1.492 and 1.496. Both trajectories have hot-to-cold temperature ratios near 1.48, consistent with an approximately inverse-temperature conductivity response over this interval. The scattering functions, modal weights, and interpolation determine the precise ratios.

The spatial spectra identify which frequencies contribute to this conductivity contrast. Fig. 7c resolves trajectory 1, and Fig. 7d resolves trajectory 2 on a common absolute scale. Existing low- and intermediate-frequency bands gain absolute conductivity toward the cold side. The fixed harmonic spectrum sets their frequency positions, while temperature-dependent relaxation changes their weights. This response links the scattering-rate decrease in Fig. 6 to enhanced conductivity within the principal heat-carrying bands. Local plateaus reflect the actual layer temperatures. The resulting all-mode conductivity field provides the reference for comparing resistance between equal-length spatial intervals.

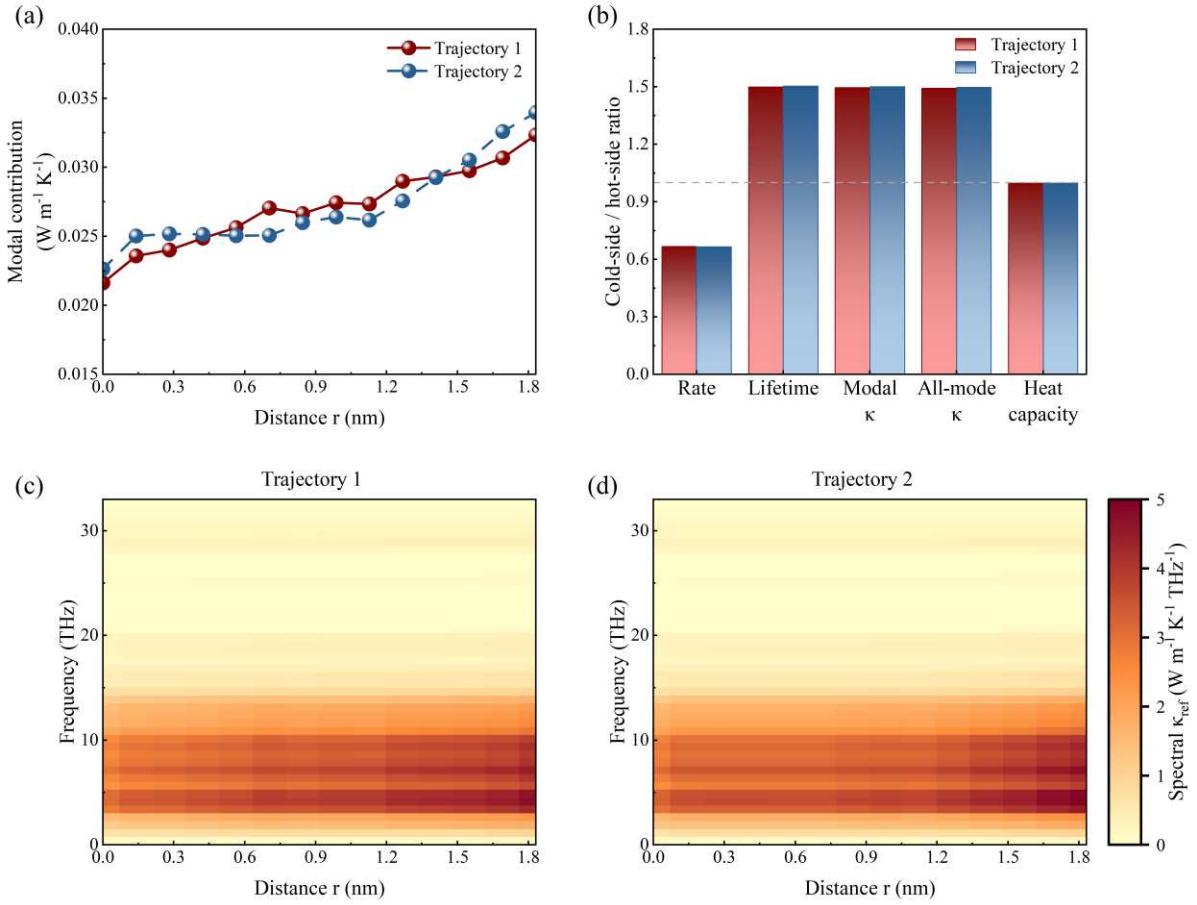


Fig. 7 Conductivity contributions within the local-temperature reference. (a) Single-mesh-point reference-mode contribution. (b) Cold-to-hot ratios of total rate, total lifetime, modal contribution, all-mode κ^{ref}, and heat capacity; the dashed line is unity. (c,d) Spatial spectra for trajectories 1 and 2 on a common absolute color scale with 0.75 THz bins. Each column is an actual layer center and integrates to κ^{ref}; no column-wise normalization is applied

The conductivity contrast changes how much resistance is assigned to equal-length intervals. Hot- and cold-endpoint κ^{ref} values are 32.35 and 48.26 W m^{-1} K^{-1} for trajectory 1, and 33.85 and 50.64 W m^{-1} K^{-1} for trajectory 2. The reference thermal resistivity $\rho^{ref}=1/\kappa_{zz}^{ref}$ in Fig. 8a decreases overall from 0.03091 to 0.02072 m K W^{-1} and from 0.02954 to 0.01975 m K W^{-1}. With equally spaced layer centers, the larger hot-side resistivity produces larger interval increments. Fig. 8b gives first and last increments of approximately 4.18×10^{-12} and 3.00×10^{-12} m^2 K W^{-1} for trajectory 1, and 3.96×10^{-12} and 2.84×10^{-12} m^2 K W^{-1} for trajectory 2.

Table 2 gives internal area-normalized reference resistances R_A^{ref} of 4.569×10^{-11} and 4.572×10^{-11} m^2 K W^{-1}. The normalized cumulative curves in Fig. 8c lie above the uniform-resistivity reference over most of the interval. They allocate 53.83% and 53.58% of the internal total to the hotter half, defined by $0\le r\le \ell/2$, where $\ell=1.832$ nm is the internal center-to-center analysis length. These shares exceed uniform allocation by 3.83 and 3.58 percentage points. The nearly equal totals coexist with different local increments inherited from the two temperature profiles.

Integrating resistivity thus quantifies how the conductivity contrast distributes reference resistance along the film.

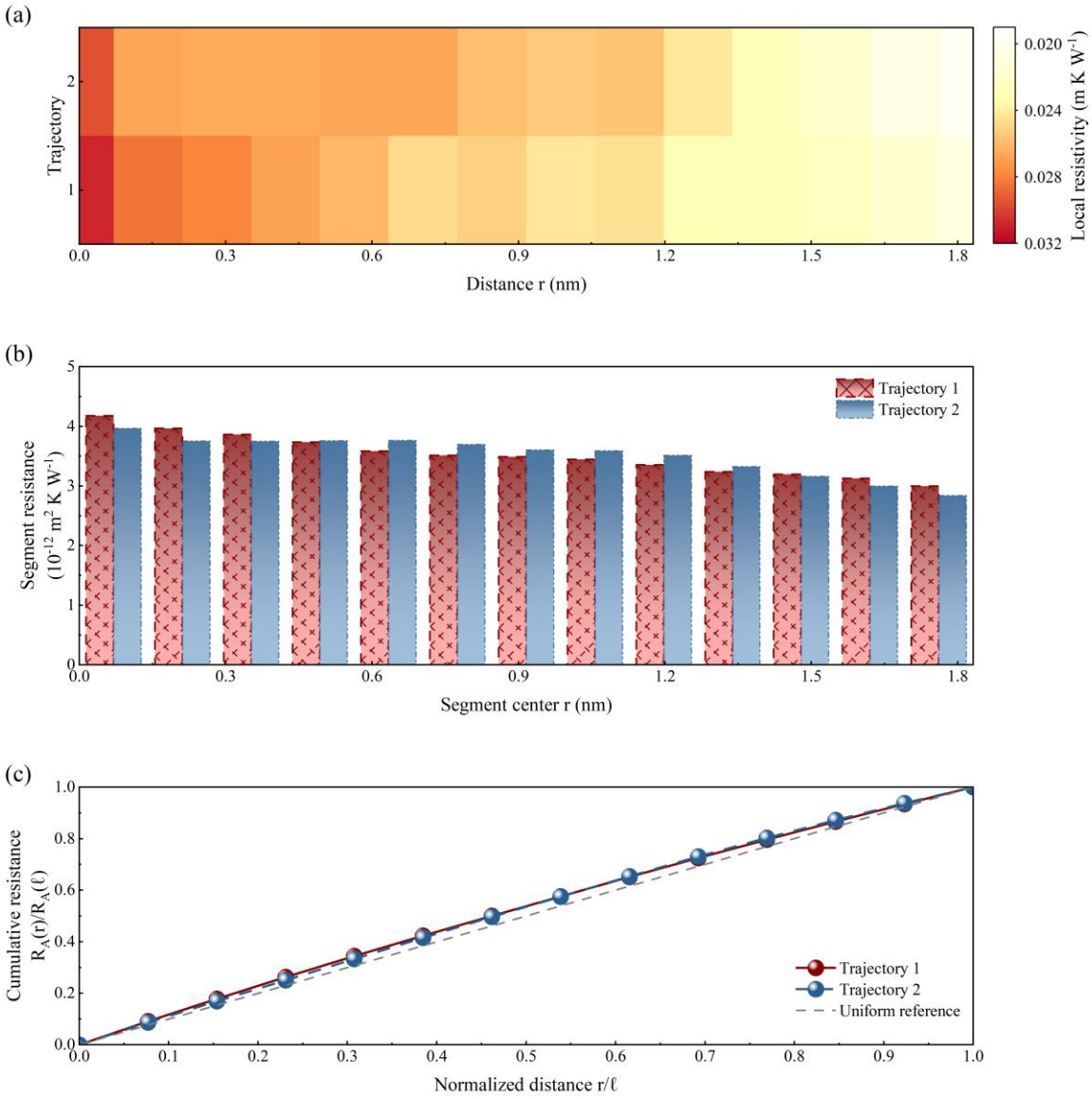


Fig. 8 Internal resistance allocation in the all-mode reference. (a) Local resistivity ρ^{ref} on a common absolute scale. (b) Area-normalized resistance increments for the 13 intervals between adjacent layer centers, plotted at interval centers. (c) Cumulative resistance normalized by the internal total; the dashed gray line is the uniform-resistivity reference. ℓ=1.832 nm

Table 2. Internal temperature fields and all-mode spatial transport references.

Trajectory	Hot/cold temperature (K)	Hot/cold κ^{ref} (W m^{-1} K^{-1})	Internal R_A^{ref} (10^{-11} m^2 K W^{-1})	Hotter-half share (%)
1	1436.24 / 971.65	32.35 / 48.26	4.569	53.83
2	1373.33 / 927.26	33.85 / 50.64	4.572	53.58

Dividing the 1.832 nm internal length by each total resistance gives an interval-equivalent conductivity reference of approximately 40.1 W m^{-1} K^{-1}. This is the harmonic spatial average of κ^{ref}, in which lower-conductivity regions receive greater weight. The higher conductivity of the cooler region consequently accompanies a concentration of resistance on the hotter side. The cumulative curve resolves this allocation spatially, identifying where model temperature-drop weight accumulates within a layer that would otherwise be represented by one averaged conductivity.

At fixed heat-flux density, the greater hot-side reference resistance gives a greater share of the model temperature drop. The two independent trajectories yield similar total reference resistances and hotter-half shares despite differences in their local temperature profiles. Their agreement supports the same overall resistance allocation for the two sampled fields. Temperature, anharmonic relaxation, conductivity contributions, and cumulative resistance are thereby related along one internal coordinate. Atomic-motion and self-consistent potential statistics characterize the microscopic hot and cold states associated with this contrast.

2.6 Spatial response of vibration and local potential

The transport reference assigns layer contrast through the thermal dependence of heat capacity and relaxation. Atomic-motion and potential signals characterize the corresponding excitation at a microscopic statistical level. Fig. 9a for Si and Fig. 9b for N both show matching principal features near 2.0 THz in the displacement spectral density S_D and relative-potential spectral density S_U, and near 5.2 THz in the velocity spectral density S_V and adjacent-step potential-change spectral density $S_{\Delta U}$. Here D, U, V, and ΔU label atomic displacement, relative electrostatic-potential signal, velocity, and potential change between successive configurations, respectively. This correspondence is consistent with the self-consistent electronic environment responding to rearrangements of the Si–N network and retaining characteristic time scales of atomic motion [37]. Secondary low-frequency features are more pronounced for Si, whereas the higher-frequency feature is more concentrated for N. Peak normalization focuses the comparison on frequencies and spectral shapes and permits signals with different units to be examined on the same frequency axis.

The two spectral correspondences emphasize configurational fluctuations and their faster temporal changes. Displacement signals resolve deviations from a mean state, while velocities and adjacent-step potential differences emphasize more rapidly varying components. Their

characteristic frequencies connect motion of the Si–N network with the self-consistent potential response. Together with the element-projected vibrational spectrum, these signals characterize shared thermal excitation with distinct local response weights for Si and N.

Beyond frequency correspondence, the nonequilibrium field resolves spatial differences in amplitude. Fig. 9c places potential root-mean-square (RMS) amplitude and relative normal-displacement RMS amplitude on the same layer coordinate. Potential RMS decreases overall from 0.3635 to 0.3052 eV for Si and from 0.4073 to 0.3472 eV for N in trajectory 1; trajectory 2 gives 0.3692 to 0.3123 eV and 0.4040 to 0.3523 eV, respectively. Cold-side values are approximately 12.8%–16.0% lower, with retained layer-scale irregularities. Symbol areas describe relative motion within each element; absolute amplitudes across Si and N require the underlying RMS values because the display references differ.

The amplitude contrast covaries with actual layer temperature. The Si states in Fig. 9d and N states in Fig. 9e give positive associations, with descriptive Pearson coefficients of approximately 0.836 and 0.928 across 28 layer states per element. Distance colors connect the higher-temperature, larger-RMS states with the hot side and the lower-amplitude states with colder layers. Local configurations and finite-time vibrational differences retain scatter at similar temperatures, giving a spatial response with both an overall thermal trend and layer-specific detail.

Individual-atom relative-potential RMS and normal-displacement RMS characterize the amplitude response of the electronic environment and structural motion, respectively. Their common layer coordinate expresses the thermal contrast in both configurational and potential fluctuations, while retaining element-specific responses. Lifetimes from anharmonic force constants resolve relaxation within the transport calculation; motion and potential statistics describe the microscopic thermal states associated with that reference.

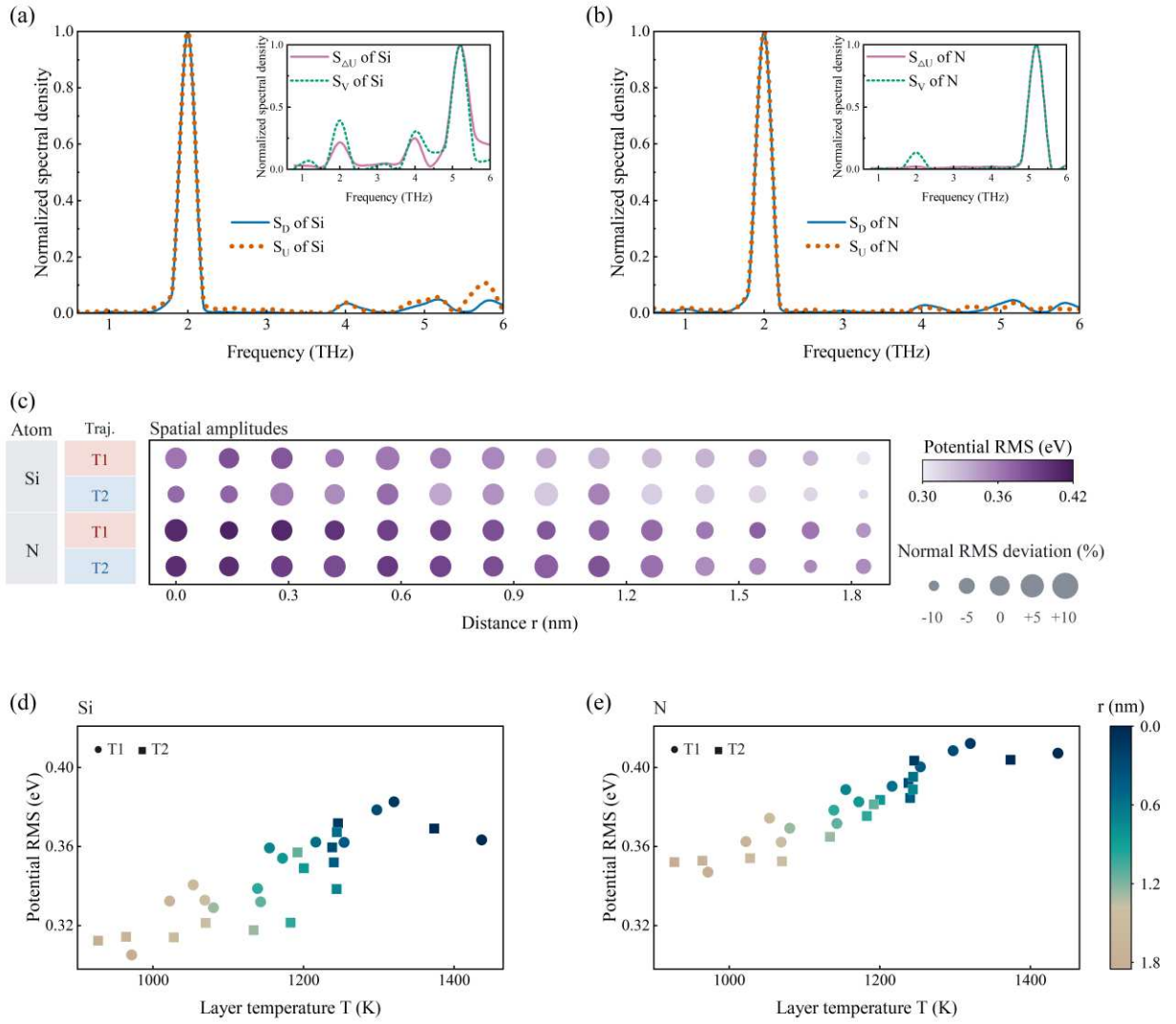


Fig. 9 Vibration–potential spectral correspondence and spatial amplitudes. (a,b) Si and N displacement S_D and relative-potential S_U spectra; insets compare velocity S_V and adjacent-step potential change $S_{\Delta U}$. Each spectrum is normalized by its own maximum. (c) The 56 element–layer–trajectory states: color is the layer mean of individual-atom relative-potential RMS; area encodes normal-displacement RMS deviation from the same-element mean, with zero percent denoting that reference. (d,e) Si and N potential RMS versus actual layer temperature; circles and squares identify the trajectories, and color gives r. Signal definitions and reference amplitudes are given under Vibration and Potential Statistics in Methods

2.7 Signal distributions and information entropy under thermal excitation

Spatial RMS amplitudes characterize differences among layers, while fixed-bin information entropy compares temporal signal distributions over a broader temperature range. The 18 group means span 315.53–1935.27 K. Fig. 10a gives a rise in the Shannon information entropy H of the Si kinetic-temperature signal from 3.690 to 6.348 bits. Fig. 10b gives a corresponding rise from 3.501 to 6.082 bits for N. The speed-signal entropies rise from 3.377 to 4.708 bits for Si and from 3.633 to 4.951 bits for N. Fixed bin widths maintain the same statistical resolution for each

signal across temperatures. Greater thermal excitation broadens these signal distributions across the fixed bins, giving the overall entropy increase.

Kinetic temperature and speed are different functions of atomic motion and have different probability distributions. Atomic mass and local bonding also distinguish the Si and N responses. Table 3 summarizes increases of 2.658 bits for the Si kinetic-temperature signal and 2.581 bits for N between the lowest and highest temperature groups. The corresponding increases for the speed signals are 1.331 and 1.318 bits. Each change describes the temperature dependence of a particular signal distribution at its specified bin width.

The information entropies of the potential and adjacent-step potential-change signals also increase overall. Potential-signal entropy rises from 3.308 to 4.170 bits for Si and from 3.292 to 4.043 bits for N. For adjacent-step potential changes, the corresponding ranges are 4.234–5.084 and 4.200–5.013 bits. These two signals describe fluctuations in the local potential and their changes between successive configurations, complementing the frequency and spatial-amplitude comparisons in Fig. 9. Both elements retain local variations around the overall thermal trend, reflecting the sampled atomic configurations and self-consistent potential fluctuations.

The equal-window analysis preserves the overall ordering with temperature, with Spearman coefficients of 0.981–1.000 across the eight element–signal curves. Each signal is compared at a common sample count across trajectories. Fixed-bin entropy describes the distribution of signal values, individual-atom RMS quantifies fluctuation amplitude, and normalized spectra identify characteristic frequencies. Together, they characterize the distributions, amplitudes, and time scales of microscopic fluctuations associated with the thermal field.

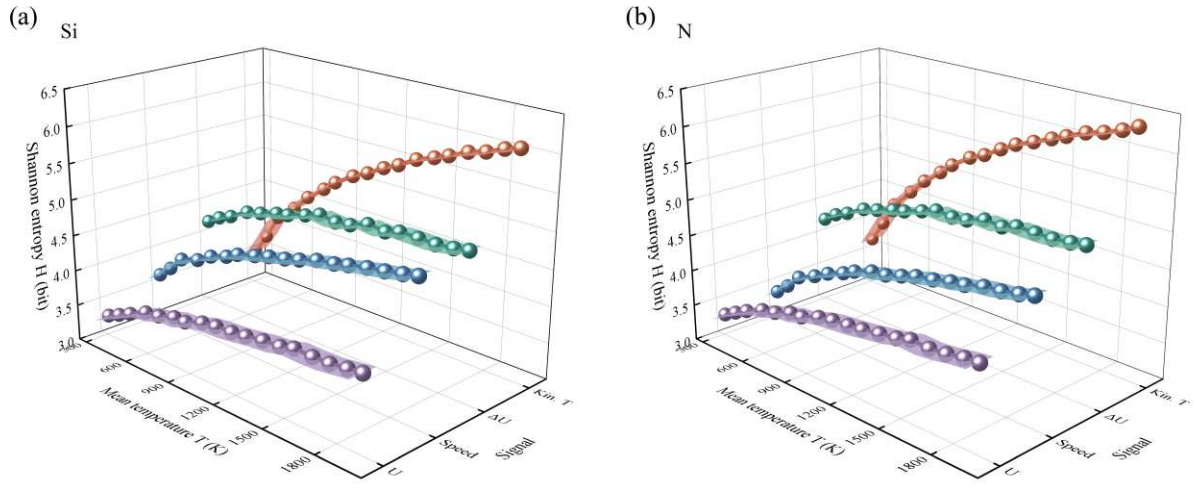


Fig. 10 Fixed-bin Shannon information entropy. (a) Si. (b) N. Symbols and lines give the means of 18 thermal-state groups formed from 49 trajectories; temperatures are actual group means. U, Speed, ΔU, and Kin. T denote element-averaged potential, speed, adjacent-step potential change, and kinetic temperature. Fixed-width ribbons identify signal categories. Binning is defined under Vibration and Potential Statistics in Methods

Table 3. Fixed-bin information entropies at the lowest and highest actual temperature groups.

Element and temperature (K)	Kinetic temperature (bits)	Speed (bits)	Potential (bits)	Adjacent-step change (bits)
Si, 315.53	3.690	3.377	3.308	4.234
Si, 1935.27	6.348	4.708	4.170	5.084
N, 315.53	3.501	3.633	3.292	4.200
N, 1935.27	6.082	4.951	4.043	5.013

Transport mapping and microscopic statistics thus provide complementary descriptions of the actual thermal states. Stronger excitation corresponds to faster three-phonon scattering and shorter lifetimes, giving hotter regions greater resistance weight within the local-temperature reference. Atomic motion and self-consistent potential describe the associated amplitude and distribution changes. The full spectrum identifies which modes carry heat, spatial integration allocates model temperature-drop weight, and signal statistics characterize the states at atomic resolution. These connections give the spatial transport contrast of a compositionally uniform film a coherent thermal interpretation.

3 Conclusions

Actual layer temperatures from two NEAIMD trajectories connect the thermal field of a 2.818 nm β-Si_3N_4 film to a mode-resolved periodic-crystal reference. Temperature drops of 446–465 K across a 1.832 nm internal interval translate into a roughly one-third decrease in the mapped three-phonon rate of a thickness-matched acoustic mode from hot to cold. Its conductivity contribution increases by approximately 50%, predominantly through the lifetime. The full mode population follows the same overall direction, while mode-count density and heat-carrying weight remain distinct.

Within the all-mode local-temperature reference, modes below 15 THz provide approximately 92% of the thermal conductivity along the film normal at the internal layers. Conductivity increases toward the cold side, and its reciprocal defines a decreasing reference thermal resistivity. Spatial integration gives an internal area-normalized reference resistance of approximately 4.57×10^{-11} m² K W^{-1}, with approximately 54% allocated to the hotter half. Modal summation followed by spatial integration connects temperature-dependent scattering to the nonuniform distribution of reference resistance and the associated model temperature-drop shares.

Vibration–potential frequency correspondence, smaller potential amplitudes toward colder layers, and increasing fixed-bin entropy with excitation characterize the associated microscopic thermal states. Actual layer temperatures connect phonon relaxation to the complete heat-carrying spectrum within the local-temperature closure. Spatial integration then resolves internal

resistance allocation, providing a mode-resolved description of conductivity contrast and model temperature-drop weight in nanoscale layers under high thermal loads.

4 Methods

4.1 Film geometry and layer temperatures

Electronic-structure calculations use the Vienna Ab initio Simulation Package (VASP) [39], the projector augmented-wave (PAW) method [40,41], and the Perdew–Burke–Ernzerhof (PBE) generalized-gradient functional [42]. The β-Si_3N_4 film contains 60 Si and 80 N atoms, with its normal parallel to the *c* axis. Periodic boundary conditions are applied in the film plane. Vacuum regions and fixed atomic layers bound the film along its normal, leaving 126 mobile atoms. The material region comprises 20 occupied slabs, each approximately 0.141 nm wide, which together define a film thickness of 2.818 nm. The cell including vacuum is approximately 3.100 nm long. Fig. 2a identifies the fixed layers and the heat-source and heat-sink regions.

NEAIMD uses microcanonical ionic dynamics in a fixed cell, with kinetic-energy exchange between source and sink atoms through virtual collisions [34,35]. The collisions preserve atomic identities and layer assignments. The time step is 1 fs, and energy exchange occurs every 40 fs. Two independent 30 ps NEAIMD simulations use different initial random velocities; their atomic trajectories are analyzed separately. A 300 eV plane-wave cutoff, an electronic iteration threshold of 10^{-5} eV, Γ-point sampling, and 0.1 eV Gaussian occupation smearing are used. Layer temperatures are calculated from kinetic energy as

$$T_i = \frac{2\langle K_i \rangle}{f_i k_B} \tag{2}$$

where K_i is the total kinetic energy of layer i, f_i is its number of dynamical degrees of freedom, and k_B is the Boltzmann constant. Temperatures are averaged over the same interval of 18.000–29.960 ps in both trajectories. The 18 layers containing mobile atoms include 14 internal analysis layers, indexed 4–17. Distance r is measured from the first internal hot-side layer center toward the cold side. The internal analysis length, denoted by ℓ, is the distance between the first and last of these 14 centers and equals 1.832 nm. Linear fits give the overall internal gradients; subsequent mappings use the actual layer means.

4.2 Isothermal phonon response and the reference mode

Second-order force constants for periodic β-Si_3N_4 are obtained by finite displacements with Phonopy [31], and third-order force constants are used in ShengBTE [32]. The force-constant calculations employ a 2×2×2 supercell, a 500 eV plane-wave cutoff, an electronic energy threshold of 10^{-8} eV, and a 5×5×11 electronic wave-vector mesh. Third-order interactions extend to the tenth-neighbor shell. Transport calculations use a 14×14×29 phonon mesh, comprising 5684 full-zone points, 510 irreducible points, and 42 branches, with nonanalytic corrections and natural-isotope scattering. Temperatures range from 200 to 2000 K in 100 K increments. All

transport quantities are evaluated within the RTA, maintaining a common lifetime definition for modal contributions and their full-spectrum sum.

For mode μ, which labels a wave vector and branch, the total scattering rate and lifetime are

$$\Gamma_\mu = \Gamma_\mu^{3ph} + \Gamma_\mu^{iso}, \quad \tau_\mu = \frac{1}{\Gamma_\mu} \tag{3}$$

The three-phonon lifetime is obtained from the three-phonon rate alone, whereas conductivity uses the total lifetime including the isotope term [38]. The Bose–Einstein mode heat capacity C_μ and RTA thermal conductivity $\kappa_{zz}^{\mathrm{RTA}}$ along the film normal are [28,32]

$$C_\mu = k_B {x_\mu}^2 \frac{e^{x_\mu}}{(e^{x_\mu}-1)^2}, \quad x_\mu = \frac{\hbar\omega_\mu}{k_B T} \tag{4}$$

$$\kappa_{\mu,zz} = \frac{C_\mu {v_{\mu,z}}^2 \tau_\mu}{N_q V_c}, \quad \kappa_{zz}^{RTA} = \sum_\mu \kappa_{\mu,zz} \tag{5}$$

Here $\hbar$ is the reduced Planck constant, ω_μ is the angular frequency, $v_{\mu,z}$ the normal group velocity, N_q the number of full-zone mesh points, and V_c the volume of the 14-atom periodic cell. A single-mode contribution carries the integration weight of one full-zone point and one branch; the reverse-wave-vector counterpart has the same contribution. The all-mode conductivity sums heat capacities, actual squared normal velocities, and corresponding total lifetimes over the complete mesh, retaining the directional tensor weights.

To compare a phonon wavelength with the material thickness, we select the third acoustic branch at reduced wave vector (0,0,3/29). This branch has longitudinal-acoustic-like character along c. On the 29-point axial mesh, this wave vector gives a wavelength $\lambda=2\pi/|q|=2.827$ nm, differing from the 2.818 nm material thickness by approximately 0.32%. The mode provides a fixed wave vector and branch for examining the temperature response at this length scale. Full-spectrum transport includes all other modes. The ShengBTE scattering-integration broadening scale factor is 1.0, with factors of 0.8 and 1.2 tested at 1200 K.

4.3 Density of states and spectral conductivity

Total and element-projected phonon densities of states are evaluated by the native linear tetrahedron method in Phonopy on a Γ-centered 41×41×41 mesh. The output spans 0–36 THz at 0.01 THz sampling intervals, with the spectral shape obtained directly from tetrahedron interpolation. Atomic projections are summed over Si or N, with target integrals of 18 and 24 states per cell, respectively, and 42 for the total. Meshes of 21×21×21, 31×31×31, and 41×41×41 are compared using the same structure and harmonic force constants as the transport model.

For the continuous conductivity spectrum, the original full-zone modal weights are distributed using normalized Gaussian kernels:

$$K_{zz}(f,T) = \sum_\mu \kappa_{\mu,zz}(T) G_\sigma(f - f_\mu), \quad G_\sigma(x) = \frac{exp[-x^2/(2\sigma^2)]}{\sqrt{(2\pi)}\sigma} \tag{6}$$

where $f_\mu=\omega_\mu/(2\pi)$, G_σ is a normalized Gaussian of standard deviation σ=0.10 THz, and the output spacing is 0.01 THz. This kernel represents discrete modal weights on a continuous frequency axis, retaining the original mode frequencies, lifetimes, and total conductivity. Frequency-band fractions and cumulative conductivities are calculated directly from the unbroadened modal sum. The spatial spectral maps retain fixed 0.75 THz bins: modal contributions in each bin are summed and divided by its width. Integration over frequency therefore recovers the all-mode conductivity. Scattering-rate and velocity scatter plots display irreducible modes, whereas mode counts and transport integrals use full-zone weights.

4.4 Local temperature mapping and rate distributions

The actual layer field T(r) supplies the link between isothermal periodic-crystal properties and internal position. Mapped modal rates, lifetimes, and contributions are defined by

$$\Gamma_\mu^{map}(r) = \Gamma_\mu[T(r)], \qquad \tau_\mu^{map}(r) = \frac{1}{\Gamma_\mu^{map}(r)} \tag{7}$$

$$\kappa_{\mu,zz}^{map}(r) = \frac{C_\mu[T(r)]v_{\mu,z}{}^2\tau_\mu^{map}(r)}{N_q V_c} \tag{8}$$

Rates are linearly interpolated between neighboring 100 K nodes before inversion, and heat capacity is recalculated at the layer temperature. The three-phonon component characterizes anharmonic scattering; total rates determine the lifetimes used for conductivity. The all-mode local-temperature reference is

$$\kappa_{zz}^{ref}(r) = \kappa_{zz}^{RTA}[T(r)], \qquad \rho^{ref}(r) = \frac{1}{\kappa_{zz}^{ref}(r)} \tag{9}$$

with linear interpolation of the isothermal all-mode conductivity. Frequency-bin contributions use the same nodes and interpolation, so summation and interpolation commute and the spectral integral agrees with κ^{ref}. Superscripts map and ref identify the mapped modal quantity and all-mode periodic-crystal reference, respectively. This closure uses T(r) as the state variable and evaluates the periodic-crystal response, with fixed harmonic properties and three-phonon plus natural-isotope scattering, at the actual layer coordinates. The resulting spatial functions compare relaxation, conductivity, and resistance at the different internal thermal states.

The distribution of three-phonon rates is estimated using a Gaussian kernel in the base-10 logarithmic coordinate $u=\log_{10}[\Gamma^{3\mathrm{ph}}/(\mathrm{ps}^{-1})]$. The kernel bandwidth is h=0.06 in this coordinate, and the resulting density is transformed to the linear rate axis. The harmonic gap at 21.1041–24.7566 THz separates modes below the gap from the high-frequency group. For frequency group b,

$$p_b(\Gamma;r) = \frac{1}{W\Gamma\, ln10}\sum_{\mu\in b} w_\mu K_h(u-u_\mu(r)) \tag{10}$$

where w_μ is the full-zone counting weight of an irreducible mode, W is the total positive-frequency weight, and K_h is a normalized Gaussian kernel. The 21417 irreducible positive-frequency modes represent 238725 full-zone modes. The group densities sum to p_Γ, which

integrates to unity at each layer; each group density integrates to its mode-count fraction. The total rate density is p_Γ, and the conditional high-frequency mode-count fraction is $F_{high}=p_{high}/p_\Gamma$. The units of p_Γ are ps, corresponding to normalized mode-count density per unit scattering rate. For the relative-rate analysis, each mode's rate is divided by its own hot-side value. The full-zone count-weighted 10th, 50th, and 90th percentiles of these ratios are denoted by P10, P50, and P90, respectively. P50 gives the median, and P10–P90 gives the range between the 10th and 90th percentiles across modes.

4.5 Reference thermal resistance

Summing all modal conductivity contributions and then taking the reciprocal defines the reference thermal resistivity, ρ^{ref}. Its integral along the internal coordinate gives the cumulative area-normalized reference resistance, with increments between adjacent layer centers [33]

$$R_A^{ref}(r) = \int_0^r \frac{dr'}{\kappa_{zz}^{ref}(r')}, \qquad \frac{dR_A^{ref}}{dr} = \rho^{ref}(r) \tag{11}$$

$$\Delta R_{A,i} = \frac{\rho^{ref}(r_i) + \rho^{ref}(r_{i+1})}{2}(r_{i+1} - r_i) \tag{12}$$

The units are m K W^{-1} for ρ^{ref} and m^2 K W^{-1} for R_A^{ref}. This reference resistance is constructed from the periodic-crystal conductivity evaluated at the actual layer temperatures. Coordinates reported in nanometers are converted to meters for the resistance integral. Trapezoidal integration produces 13 increments from the 14 internal layer centers. Cumulative resistance is normalized by its internal total, with the hotter half defined by $0 \le r \le \ell/2$. Modal contributions are summed within each layer before the inverse conductivity is integrated along the heat-transfer direction. Under a steady one-dimensional description using this local-temperature reference, each interval's temperature drop equals its area-normalized resistance multiplied by a constant heat-flux density. The resistance shares therefore give the model temperature-drop shares.

4.6 Vibration and potential statistics

Vibration–potential spectra are obtained from atomic-motion and ionic-core-potential signals in fixed-cell *ab initio* molecular dynamics (AIMD) [37]. These trajectories employ Nosé–Hoover temperature control, a 1 fs step, and 10000 steps, with a temperature scan covering 300, 600, 900, 1200, and 1500 K. The spectral densities of atomic displacement D, relative electrostatic-potential signal U, velocity V, and adjacent-step potential change ΔU are denoted by S_D, S_U, S_V, and $S_{\Delta U}$, respectively. The autocorrelation–Fourier relation is written as

$$S_X(f) \propto |\mathcal{F}\{R_X(t)\}|, \qquad R_X(t) = \langle X(t_0)X(t_0+t)\rangle \tag{13}$$

Here R_X is the autocorrelation function of signal X, t is the time lag, t_0 is a time origin, and $\mathcal{F}$ denotes the Fourier transform. Each spectrum is normalized to its own maximum for frequency and shape comparisons. U denotes the local electrostatic-potential signal at an ionic core. ΔU is the difference between successive configurations separated by 1 fs and retains units of potential.

For nonequilibrium spatial statistics, the instantaneous mean potential of all mobile atoms is subtracted from each ionic-core potential φ_j(t), followed by removal of the temporal mean of that relative signal:

$$\delta\varphi_j(t) = \varphi_j(t) - \bar{\varphi}_{mob}(t) - \langle\varphi_j(t) - \bar{\varphi}_{mob}(t)\rangle \quad (14)$$

$$u_\alpha(r) = \frac{1}{n_{\alpha,r}}\sum_{j\in\alpha,r}\langle\delta{\varphi_j}^2\rangle^{1/2} \quad (15)$$

Here j labels an atom, α denotes Si or N, $n_{\alpha,r}$ is the number of atoms of element α in the initial layer at r, $\bar{\varphi}_{\mathrm{mob}}$ is the instantaneous mean potential over mobile atoms, and angle brackets denote time averaging. The quantity u_α(r) is the arithmetic mean of individual-atom root-mean-square (RMS) amplitudes within that element and layer. Displacement RMS along the film normal is likewise calculated for each atom relative to its time-mean position before element–layer averaging. Both quantities use the 14 internal layers and the 18.000–29.960 ps window. In the amplitude comparison, color encodes absolute potential RMS. Symbol area represents the percentage deviation of normal-displacement RMS from the mean of the 28 layer states of the same element, using an affine mapping. The Si and N reference amplitudes are 0.00818 and 0.00966 nm, respectively. Symbol areas thus compare relative spatial differences within each element.

Shannon information entropy is evaluated for element-averaged kinetic temperature, atomic speed (velocity magnitude), potential, and adjacent-step potential change in 49 trajectories spanning 18 thermal-state groups [43]:

$$H(X) = -\sum_b p_b log_2 p_b\,, \quad p_b = \frac{n_b}{N} \quad (16)$$

In the entropy expression, n_b is the number of samples in bin b and N is the total sample count. Element averaging is performed at each time step before the probabilities are accumulated. For the speed signal, the velocity magnitude is calculated for each atom before averaging over atoms of the same element. Bin widths are 10 K, 0.01 nm ps^{-1}, 0.01 eV, and 0.001 eV for temperature, speed, potential, and adjacent-step potential change, respectively. The width and bin boundaries are fixed for each signal across temperatures. Entropy is calculated separately for each trajectory and then averaged arithmetically over the 1–3 trajectories in a group; the temperature coordinate is the group's actual mean. An equal-window check uses 9961 consecutive configurations per trajectory. These yield 9961 samples for temperature, speed, and potential, and 9960 adjacent-step potential differences. H, in bits, measures probability-distribution uncertainty for the specified signal and statistical resolution. Thermal trends are evaluated within each signal at fixed binning, using the same corresponding definitions for Si and N.

4.7 AI-assisted manuscript preparation

OpenAI Codex assisted language revision, manuscript organization, consistency checks, and document/source-file preparation. The Scientific Writing workflow in Scientific Agent Skills supported local consistency checks. OpenAI image-generation tools assisted the conceptual

artwork in Figs. 1 and 3 from the author-developed physical setting and qualitative scattering description. These two illustrations depict the conceptual setting and scattering mechanism. Numerical results and data plots originate from the computational analyses described in this work.

Software-workflow reference: Kassis T, Agarwal V, He Y, Patel D, Brueckner AM (2026) Scientific Agent Skills: A Library of Procedural Knowledge for Research Agents. arXiv:2609.00065. https://doi.org/10.48550/arXiv.2609.00065

Supplementary information

Online Resource 1 (PDF): Model dimensions, numerical conventions, layer-temperature statistics, temporal-block analysis, scattering-integration broadening sensitivity, density-of-states mesh comparisons, equal-window information-entropy analysis, transport integration, symbol definitions, and numerical tables.

Online Resource 2 (ZIP): Tabulated results, analysis scripts, periodic-crystal force constants and phonon outputs, and input structures.

References

1. Padture NP, Gell M, Jordan EH (2002) Thermal Barrier Coatings for Gas-Turbine Engine Applications. Science 296:280-284. https://doi.org/10.1126/science.1068609

2. Clarke DR, Levi CG (2003) Materials Design for the Next Generation Thermal Barrier Coatings. Annu. Rev. Mater. Res. 33:383-417. https://doi.org/10.1146/annurev.matsci.33.011403.113718

3. Cao XQ, Vassen R, Stoever D (2004) Ceramic materials for thermal barrier coatings. J. Eur. Ceram. Soc. 24:1-10. https://doi.org/10.1016/s0955-2219(03)00129-8

4. Evans AG, Mumm DR, Hutchinson JW, Meier GH, Pettit FS (2001) Mechanisms controlling the durability of thermal barrier coatings. Prog. Mater. Sci. 46:505-553. https://doi.org/10.1016/s0079-6425(00)00020-7

5. Yvon P, Carré F (2009) Structural materials challenges for advanced reactor systems. J. Nucl. Mater. 385:217-222. https://doi.org/10.1016/j.jnucmat.2008.11.026

6. Akiyoshi M, Takagi I, Yano T, Akasaka N, Tachi Y (2006) Thermal conductivity of ceramics during irradiation. Fusion Eng. Des. 81:321-325. https://doi.org/10.1016/j.fusengdes.2005.08.084

7. Terricabras AJ, Ferrigno J, Wang L, Khafizov M, Nelson AT, Zinkle SJ (2022) Thermal conductivity evaluation of ion irradiated Si_3N_4 and ZrN ceramics using spatial domain thermoreflectance. J. Appl. Phys. 132:075105. https://doi.org/10.1063/5.0099175

8. Riley FL (2000) Silicon Nitride and Related Materials. J. Am. Ceram. Soc. 83:245-265. https://doi.org/10.1111/j.1151-2916.2000.tb01182.x

9. Klemm H (2010) Silicon Nitride for High-Temperature Applications. J. Am. Ceram. Soc. 93:1501-1522. https://doi.org/10.1111/j.1551-2916.2010.03839.x

10. Wiederhorn SM, Ferber MK (2001) Silicon nitride for gas turbines. Curr. Opin. Solid State Mater. Sci. 5:311-316. https://doi.org/10.1016/S1359-0286(00)00032-2

11. Bocanegra-Bernal MH, Matovic B (2010) Mechanical properties of silicon nitride-based ceramics and its use in structural applications at high temperatures. Mater. Sci. Eng. A 527:1314-1338. https://doi.org/10.1016/j.msea.2009.09.064

12. Blugan G, Wittig D, Kuebler J (2009) Oxidation and corrosion of silicon nitride ceramics with different sintering additives at 1200 and 1500°C in air, water vapour, SO_2 and HCl environments – A comparative study. Corros. Sci. 51:547-555. https://doi.org/10.1016/j.corsci.2008.12.014

13. Opila EJ (2003) Oxidation and Volatilization of Silica Formers in Water Vapor. J. Am. Ceram. Soc. 86:1238-1248. https://doi.org/10.1111/j.1151-2916.2003.tb03459.x

14. Evans AG, Hutchinson JW (1995) The thermomechanical integrity of thin films and multilayers. Acta Metall. Mater. 43:2507-2530. https://doi.org/10.1016/0956-7151(94)00444-m

15. Hirao K, Watari K, Brito ME, Toriyama M, Kanzaki S (1996) High Thermal Conductivity in Silicon Nitride with Anisotropic Microstructure. J. Am. Ceram. Soc. 79:2485-2488. https://doi.org/10.1111/j.1151-2916.1996.tb09002.x

16. Kitayama M, Hirao K, Tsuge A, Watari K, Toriyama M, Kanzaki S (2000) Thermal Conductivity of β-Si_3N_4: II, Effect of Lattice Oxygen. J. Am. Ceram. Soc. 83:1985-1992. https://doi.org/10.1111/j.1151-2916.2000.tb01501.x

17. Yokota H, Ibukiyama M (2003) Effect of lattice impurities on the thermal conductivity of β-Si_3N_4. J. Eur. Ceram. Soc. 23:55-60. https://doi.org/10.1016/s0955-2219(02)00074-2

18. Yokota H, Abe H, Ibukiyama M (2003) Effect of lattice defects on the thermal conductivity of β-Si_3N_4. J. Eur. Ceram. Soc. 23:1751-1759. https://doi.org/10.1016/s0955-2219(02)00374-6

19. Hirosaki N, Ogata S, Kocer C, Kitagawa H, Nakamura Y (2002) Molecular dynamics calculation of the ideal thermal conductivity of single-crystal α- and β-Si_3N_4. Phys. Rev. B 65:134110. https://doi.org/10.1103/physrevb.65.134110

20. Zhou H, Feng T (2023) Theoretical upper limits of the thermal conductivity of Si_3N_4. Appl. Phys. Lett. 122:182203. https://doi.org/10.1063/5.0149298

21. Li Y, Duan X, Fu Z, Zhao H, He YL, Lu XL, Yang JY, Ma XH (2023) Intrinsic electron mobility and lattice thermal conductivity of β-Si_3N_4 from first-principles. Solid State Commun. 361:115066. https://doi.org/10.1016/j.ssc.2023.115066

22. Cahill DG, Ford WK, Goodson KE, Mahan GD, Majumdar A, Maris HJ, Merlin R, Phillpot SR (2003) Nanoscale thermal transport. J. Appl. Phys. 93:793-818. https://doi.org/10.1063/1.1524305

23. Cahill DG, Braun PV, Chen G, Clarke DR, Fan S, Goodson KE, Keblinski P, King WP, Mahan GD, Majumdar A, Maris HJ, Phillpot SR, Pop E, Shi L (2014) Nanoscale thermal transport. II. 2003–2012. Appl. Phys. Rev. 1:011305. https://doi.org/10.1063/1.4832615

24. Bogner M, Hofer A, Benstetter G, Gruber H, Fu RYQ (2015) Differential 3ω method for measuring thermal conductivity of AlN and Si_3N_4 thin films. Thin Solid Films 591:267-270. https://doi.org/10.1016/j.tsf.2015.03.031

25. Alam MT, Manoharan MP, Haque MA, Muratore C, Voevodin AA (2012) Influence of strain on thermal conductivity of silicon nitride thin films. J. Micromech. Microeng. 22:045001. https://doi.org/10.1088/0960-1317/22/4/045001

26. Shen N, Wu X, Li L, Liang X (2025) Amorphous Silicon Nitride Thin Film Withstanding Up to 1700 °C: Structure and Thermal Conductivity. J. Phys. Chem. Lett. 16:6385-6392. https://doi.org/10.1021/acs.jpclett.5c01552

27. Huang D, Lyu J, Wu Z, Tang G, Yang L (2026) Thermal conductivity modulation under strain gradients in III–V semiconductors. Appl. Surf. Sci. 735:166672. https://doi.org/10.1016/j.apsusc.2026.166672

28. Ward A, Broido DA, Stewart DA, Deinzer G (2009) Ab initio theory of the lattice thermal conductivity in diamond. Phys. Rev. B 80:125203. https://doi.org/10.1103/physrevb.80.125203

29. Feng T, Lindsay L, Ruan X (2017) Four-phonon scattering significantly reduces intrinsic thermal conductivity of solids. Phys. Rev. B 96:161201. https://doi.org/10.1103/physrevb.96.161201

30. Li Z, Ouyang T, Han L, Tang Z, Wang X, Cao J, Zhang P, Yao Y, Wei X (2025) Impact of high-order anharmonicity and nitrogen vacancy defects on the thermal conductivity of $MoSi_2N_4$. Phys. Rev. B 112:064309. https://doi.org/10.1103/gmh7-gsk8

31. Togo A, Tanaka I (2015) First principles phonon calculations in materials science. Scr. Mater. 108:1-5. https://doi.org/10.1016/j.scriptamat.2015.07.021

32. Li W, Carrete J, Katcho NA, Mingo N (2014) ShengBTE: A solver of the Boltzmann transport equation for phonons. Comput. Phys. Commun. 185:1747-1758. https://doi.org/10.1016/j.cpc.2014.02.015

33. Baehr HD, Stephan K (2011) Heat and Mass Transfer. Springer, Berlin, Heidelberg. https://doi.org/10.1007/978-3-642-20021-2

34. Müller-Plathe F (1997) A simple nonequilibrium molecular dynamics method for calculating the thermal conductivity. J. Chem. Phys. 106:6082-6085. https://doi.org/10.1063/1.473271

35. Yue SY, Zhang X, Stackhouse S, Qin G, Di Napoli E, Hu M (2016) Methodology for determining the electronic thermal conductivity of metals via direct nonequilibrium ab initio molecular dynamics. Phys. Rev. B 94:075149. https://doi.org/10.1103/physrevb.94.075149

36. Yue SY, Hu M (2019) Insight of the thermal conductivity of ϵ-iron at Earth's core conditions from the newly developed direct ab initio methodology. J. Appl. Phys. 125:045102. https://doi.org/10.1063/1.5055389

37. Huang D, Tang G, Gao Z, Yue S (2025) The effect of atomic vibration on thermal transport in diatomic semiconductors investigated via ab initio molecular dynamics. Nanoscale 17:2878-2888. https://doi.org/10.1039/d4nr05240d

38. Tamura Si (1983) Isotope scattering of dispersive phonons in Ge. Phys. Rev. B 27:858-866. https://doi.org/10.1103/physrevb.27.858

39. Kresse G, Furthmüller J (1996) Efficient iterative schemes for ab initio total-energy calculations using a plane-wave basis set. Phys. Rev. B 54:11169-11186. https://doi.org/10.1103/physrevb.54.11169

40. Blöchl PE (1994) Projector augmented-wave method. Phys. Rev. B 50:17953-17979. https://doi.org/10.1103/physrevb.50.17953

41. Kresse G, Joubert D (1999) From ultrasoft pseudopotentials to the projector augmented-wave method. Phys. Rev. B 59:1758-1775. https://doi.org/10.1103/physrevb.59.1758

42. Perdew JP, Burke K, Ernzerhof M (1996) Generalized Gradient Approximation Made Simple. Phys. Rev. Lett. 77:3865-3868. https://doi.org/10.1103/physrevlett.77.3865

43. Shannon CE (1948) A Mathematical Theory of Communication. Bell Syst. Tech. J. 27:379-423. https://doi.org/10.1002/j.1538-7305.1948.tb01338.x

Supplementary Files

This is a list of supplementary files associated with this preprint. Click to download.

- ESM1.pdf
- ESM2.zip